

# The Effect of Evanescent Modes and Chaos on Deterministic Scattering in an Electron Waveguide.

G.B. Akguc and L.E. Reichl  
Center for Studies in Statistical Mechanics and Complex Systems  
The University of Texas at Austin  
Austin, Texas 78712

October 29, 2018

## Abstract

Statistical properties of Wigner delay times and the effect of evanescent modes on the deterministic scattering of an electron matter wave from a classically chaotic 2-d electron waveguide are studied for the case of 2, 6, and 16 propagating modes. Deterministic reaction matrix theory for this system is generalized to include the effect of evanescent modes on the scattering process. The statistical properties of the Wigner delay times for the deterministic scattering process are compared to the predictions of random reaction matrix theory.

PACS numbers : 05.45.Mt, 05.60.Gg, 73.23.Ad, 73.50.Bk

## 1 Introduction

In the 1950's it was observed that nuclear scattering processes can have statistical properties indistinguishable from random scattering processes [1]. The first hint that these random elements in the nuclear scattering data might be due to underlying chaos in the nuclear dynamics appeared in a paper by McDonald and Kauffman [2] who studied the energy level statistics for closed quantum billiards whose classical counterparts are either integrable or chaotic. They found that

the quantized energy levels of the chaotic billiard had a statistical distribution which matched predictions of random matrix theory. The first studies of the scattering properties of completely chaotic quantum systems with few degrees of freedom were due to Smilansky [3] and since then a number of papers have appeared [4],[5] analysing quantum scattering using semi-classical techniques [6],[7],[8], and focused on the semiclassical regime. Recently Akguc and Reichl [9] studied deterministic quantum scattering from a chaotic billiard, in a regime where only a few channels are open, using finite elements techniques and have found random signatures in the Wigner delay times.

The analysis of fully quantum mechanical scattering processes, in systems where only a few channels are open, is not easily accessible because this regime is numerically demanding. This fact has led to renewed interest in the reaction matrix formulation of scattering theory that was developed by Wigner and Eisenbud [10] in the late 1940's [11]. The idea behind reaction matrix theory is to decompose configuration space into a reaction region (cavity) and an asymptotic scattering region (lead). The exact wavefunction in the reaction region can be expanded in terms of any convenient complete set of states with fixed boundary conditions on the surface of the reaction region, provided the coupling between the reaction region (cavity) and asymptotic scattering region is singular [12], [13]. Reaction matrix theory provides a convenient framework for predicting the scattering properties of systems governed by random Hamiltonian matrices. We shall call the theory that uses reaction matrix theory to predict the scattering properties of systems with Gaussian random Hamiltonians, *random reaction matrix theory* or RRMT. The predictions of RRMT have been compared to experimental nuclear scattering data [15], scattering in electron waveguides [16], and resonances in acoustic and micro-wave resonators [17], under conditions in which these systems are thought to have classically chaotic dynamics. These predictions, in turn, can be compared to the scattering properties of chaotic systems. RRMT, as it is currently formulated, neglects some possibly impor-

tant effects in the scattering process, namely the effect of evanescent modes and some of the energy dependence of resonance poles.

In this paper, we will study the deterministic scattering of an electron in a two dimensional electron waveguide, which has a classically chaotic cavity formed by a ripple billiard connected to a lead at one end (see Figure 1). This type of cavity is particularly well suited to the use of reaction matrix theory, because a simple coordinate transformation allows us to construct the basis states inside the cavity by diagonalizing a Hamiltonian matrix. We will generalize the reaction matrix theory for two dimensional waveguides to include the effect of evanescent modes. The effect of evanescent modes on scattering processes has been studied for nuclear scattering processes [18],[19],[20],[21] using approximate theories. For electron waveguides, we can include these effects exactly. We will show that for the waveguide we consider, evanescent modes dominate the scattering properties of the waveguide in energy regions where new propagating channels open. We will also compare the statistical properties of Wigner delay times for the deterministic waveguide scattering process to the predictions of RRMT.

We begin, in Section 2, by developing the reaction matrix theory of deterministic scattering in our electron waveguide, starting from a configuration space formulation rather than the usual eigenmode formulation, and we construct the Hamiltonians for the cavity (reaction region) and leads (asymptotic scattering region) of an electron waveguide. In Section (3) (and Appendix A) we use the hermiticity of the total Hamiltonian to compute the strength of the coupling between the cavity and lead. In Section (4), we derive the reaction matrix. In Section (5), we derive the scattering matrix. In Section (6), we describe the method we use to obtain a complete set of basis states for a cavity with a rippled wall. In Section (7) we discuss the accuracy of the reaction matrix predictions by comparing them with a finite element calculation. In Section (8), we discuss the effect of evanescent modes on the scattering process, and in Section (9) we

compare the statistical properties of the Wigner delay times for deterministic scattering in the waveguide with predictions of RRMT. Finally, in Section (10), we make some concluding remarks.

## 2 Scattering Hamiltonian

We will consider the scattering properties of an electron with mass,  $m$ , in the waveguide shown in Fig. (1). The electron enters from the left with energy  $E$  along an infinitely long straight lead which has infinitely hard walls. The electron wave is reflected back to the left by an infinitely hard wall located at  $x = 0$ . The scattering is strongly affected by the region  $0 < x < L$  (the cavity) in which the upper wall is rippled.

The Schrodinger equation, which describes propagation of a particle wave,  $\Psi(x, y, t)$ , for all times,  $t$ , is given by

$$i\hbar \frac{\partial \Psi(x, y, t)}{\partial t} = \left[ -\frac{\hbar^2}{2m} \left( \frac{\partial^2}{\partial x^2} + \frac{\partial^2}{\partial y^2} \right) + V(x, y) \right] \Psi(x, y, t), \quad (1)$$

where  $\hbar$  is Planck's constant. The potential,  $V(x, y)$ , has the following properties:  $V(x, y) = \infty$  for  $(L \leq x < \infty)$ ;  $V(x, 0) = \infty$  for  $(-\infty \leq x \leq L)$ ;  $V(x, y = g(x)) = \infty$  for  $(0 < x < L)$ ; and  $V(x, y = a + d) = \infty$  for  $(-\infty < x < 0)$ ; where  $g(x) = d + a \cos(4\pi x/L)$  gives the contour of the ripple,  $d$  is the average width of the cavity,  $L$  is the length, and  $a$  is the ripple amplitude. Throughout this paper, we take the electron mass to be the effective mass of an electron in GaAs,  $m = 0.067m_e$ , where  $m_e$  is the free electron mass.

We can introduce projection operators,  $\hat{P} = \int_{-\infty}^0 dx \int_{-\infty}^{\infty} dy |x, y\rangle \langle x, y|$  and  $\hat{Q} = \int_0^L dx \int_{-\infty}^{\infty} dy |x, y\rangle \langle x, y|$  which satisfy the completeness relation  $\hat{Q} + \hat{P} = \hat{1}$  (all wavefunctions are zero for  $L < x$ ). Here  $|x, y\rangle$  is the simultaneous eigenstate of position operators,  $\hat{x}$  and  $\hat{y}$ . The projection operators,  $\hat{Q}$  and  $\hat{P}$  have the property that  $\hat{Q} = \hat{Q}^2$ ,  $\hat{P} = \hat{P}^2$ , and  $\hat{Q}\hat{P} = \hat{P}\hat{Q} = 0$ . If a state,  $|\Psi\rangle$  has spatial dependence,  $\Psi(x, y) \equiv \langle x, y | \Psi \rangle$ , over the interval  $(-\infty < x < L)$ , then the state

$\langle x, y | \hat{Q} | \Psi \rangle = \Psi(x, y)$  for  $(0 < x < L)$  and the state  $\langle x, y | \hat{P} | \Psi \rangle = \Psi(x, y)$  for  $(-\infty < x < 0)$ .

Inside the cavity (Region I,  $(0 < x < L)$  in Fig.(1)), we define a Hamiltonian,

$$\hat{H}_{QQ} \equiv \hat{Q} \left[ \frac{1}{2m} (\hat{p}_x^2 + \hat{p}_y^2) + V(x, y) \right] \hat{Q}, \quad (2)$$

where  $\hat{p}_x$  and  $\hat{p}_y$  are momentum operators and  $m$  is the mass of the particle. The Hamiltonian,  $\hat{H}_{QQ}$ , is Hermitian and therefore it will have a complete, orthonormal set of eigenstates which we denote as  $\hat{Q} |\phi_j\rangle$ . We can write the eigenvalue equation in the region,  $0 < x < L$ , as  $\hat{H}_{QQ} \hat{Q} |\phi_j\rangle = \lambda_j \hat{Q} |\phi_j\rangle$ , where  $\lambda_j$  is the  $j^{th}$  energy eigenvalue of  $\hat{H}_{QQ}$  and  $j = 1, 2, \dots, M$  (we will later let  $M \rightarrow \infty$ ). Because there is an infinitely hard wall at  $x = L$ , the eigenstates  $\phi_j(x, y) \equiv \langle x, y | \hat{Q} |\phi_j\rangle$  must be zero at  $x = L$ . We have some freedom in choosing the boundary condition at  $x = 0$ . In this paper, we will require that the eigenstates,  $\phi_j(x, y)$ , have zero slope at  $x = 0$  so that  $\frac{d\phi_j}{dx} \Big|_{x=0} = 0$ . Singular coupling, between the cavity and the lead, will correct for the fact that the actual wavefunction does not have zero slope at  $x = 0$ . The completeness of the states,  $\hat{Q} |\phi_j\rangle$ , allows us to write the completeness relation,  $\sum_j \hat{Q} |\phi_j\rangle \langle \phi_j | \hat{Q} = \hat{Q}$ . Orthonormality requires that  $\langle \phi_j | \hat{Q} |\phi_{j'}\rangle = \delta_{j,j'}$ . The part, inside the cavity, of any state,  $|\Psi\rangle$ , in the waveguide can be expanded in terms of this complete set of states, so that

$$\hat{Q} |\Psi\rangle = \sum_{j=1}^M \langle \phi_j | \hat{Q} |\Psi\rangle |\phi_j\rangle. \quad (3)$$

Inside the lead (Region II,  $(-\infty < x < 0)$  in Fig. (1)), we define a Hamiltonian

$$\hat{H}_{PP} \equiv \hat{P} \left[ \frac{1}{2m} (\hat{p}_x^2 + \hat{p}_y^2) + V(x, y) \right] \hat{P}. \quad (4)$$

Its eigenvalues are continuous and have range,  $(0 \leq E \leq \infty)$ . The eigenvector of  $\hat{H}_{PP}$ , with eigenvalue,  $E$ , will be denoted  $\hat{P} |E\rangle$ . The eigenvalue equation then reads,  $\hat{H}_{PP} \hat{P} |E\rangle = E \hat{P} |E\rangle$ . Because the leads are assumed to be straight, the transverse parts of the energy eigenstates, in the leads, decouple from the

longitudinal part. Because the walls of the channels are infinitely hard, the energy eigenstates in the leads (for  $x < 0$ ) can be written

$$\hat{P}|E\rangle = \sum_{n=0}^N \Gamma_n \hat{P}|\Phi_n\rangle, \quad (5)$$

where  $\Gamma_n = \langle \Phi_n | \hat{P} | E \rangle$  and

$$\langle x, y | \hat{P} | \Phi_n \rangle = \chi_{k,n}(x) \sqrt{\frac{2}{d+a}} \sin\left(\frac{n\pi y}{d+a}\right) \quad (6)$$

represents the contribution to  $\langle x | E \rangle$  from the  $n^{\text{th}}$  transverse quantum state in the lead. Although we have summed over the first  $N$  transverse states we will later let  $N \rightarrow \infty$ . For a particle with energy,  $E$ , the state,  $\hat{P}|\Phi_n\rangle$ , has the property that

$$\hat{H}_{PP} \hat{P}|\Phi_n\rangle = E \hat{P}|\Phi_n\rangle = \frac{\hbar^2}{2m} \left( k_n^2 + \left( \frac{n\pi}{d+a} \right)^2 \right) \hat{P}|\Phi_n\rangle. \quad (7)$$

where

$$E = \frac{\hbar^2}{2m} \left( k_n^2 + \left( \frac{n\pi}{d+a} \right)^2 \right). \quad (8)$$

The state,  $\hat{P}|\Phi_n\rangle$  is called the  $n^{\text{th}}$  channel. Eq. (8) gives the decomposition of the total energy,  $E$ , into its longitudinal and transverse parts when the electron is in the channel,  $\hat{P}|\Phi_n\rangle$ . For a given energy,  $E$ , there are an infinite number of channels for the particle, some propagating and some evanescent. Channels with propagating modes occur if the longitudinal wavevector is real. Channels with evanescent modes occur if the longitudinal wavevector is pure imaginary. Evanescent modes describe localized contributions to the electron states in the waveguide. There are an infinite number of them and for some values of the energy,  $E$ , they play a dominant role in determining the dynamics in the waveguide [25].

We couple the cavity and the lead at their interface,  $x = 0$ , via the singular operator,  $\hat{V} = C\delta(\hat{x})\hat{p}_x$ . The coupling constant,  $C$ , can be determined by the

condition that the total Hamiltonian [14] be Hermitian (see Section (3)). Then

$$\hat{H}_{QP} = \hat{Q}\hat{V}\hat{P} = C\frac{\hbar}{i}\int_0^L dx_1 \int_{-\infty}^{\infty} dy_1 \int_{-\infty}^0 dx_0 |x_1, y_1\rangle\delta(x_1 - x_0)\delta(x_0)\frac{d}{dx_0}\langle x_0, y_1|, \quad (9)$$

and

$$\hat{H}_{PQ} = \hat{P}\hat{V}\hat{Q} = C\frac{\hbar}{i}\int_{-\infty}^0 dx_0 \int_{-\infty}^{\infty} dy_0 \int_0^L dx_1 |x_0, y_0\rangle\delta(x_0 - x_1)\delta(x_1)\frac{d}{dx_1}\langle x_1, y_0|. \quad (10)$$

It is useful to remember that  $\int_0^L dx \delta(x) = \frac{1}{2}$ ,  $\int_0^L dx \delta(x - x_0) = 1$  if  $0 < x_0 < L$ , and  $\int_0^L dx \delta(x - x_0) = 0$  if  $L < x_0$  or  $x_0 < 0$ . Note also that

$$\hat{H}_{QQ} = \int_0^L dx \int_{-\infty}^{\infty} dy |x, y\rangle\frac{-\hbar^2}{2m}\left(\frac{d^2}{dx^2} + \frac{d^2}{dy^2} + V(x, y)\right)\langle x, y|, \quad (11)$$

and

$$\hat{H}_{PP} = \int_{-\infty}^0 dx \int_{-\infty}^{\infty} dy |x, y\rangle\frac{-\hbar^2}{2m}\left(\frac{d^2}{dx^2} + \frac{d^2}{dy^2} + V(x, y)\right)\langle x, y| \quad (12)$$

The total Hamiltonian of the system can be written

$$\hat{H} = \hat{H}_{QQ} + \hat{H}_{PP} + \hat{H}_{QP} + \hat{H}_{PQ}. \quad (13)$$

The waveguide energy eigenstates,  $|E\rangle$ , satisfy the eigenvalue equation  $\hat{H}|E\rangle = E|E\rangle$ . The states,  $|E\rangle$ , can be decomposed into their contributions from the two regions of configuration space, so that

$$|E\rangle = \sum_{j=1}^M \gamma_j \hat{Q}|\phi_j\rangle + \sum_{n=0}^N \Gamma_n \hat{P}|\Phi_n\rangle, \quad (14)$$

where  $\gamma_j = \langle\phi_j|\hat{Q}|E\rangle$  and  $\Gamma_n = \langle\Phi_n|\hat{P}|E\rangle$ . The eigenvalue equation then takes the form

$$\begin{pmatrix} \hat{H}_{QQ} & 0 & \dots & \hat{H}_{QP} & \hat{H}_{QP} & \dots \\ 0 & \hat{H}_{QQ} & \dots & \hat{H}_{QP} & \hat{H}_{QP} & \dots \\ \vdots & \vdots & \ddots & \vdots & \vdots & \dots \\ \hat{H}_{PQ} & \hat{H}_{PQ} & \dots & \hat{H}_{PP} & 0 & \dots \\ \hat{H}_{PQ} & \hat{H}_{PQ} & \dots & 0 & \hat{H}_{PP} & \dots \\ \vdots & \vdots & \dots & \vdots & \vdots & \dots \end{pmatrix} \begin{pmatrix} \gamma_1 \hat{Q}|\phi_1\rangle \\ \gamma_2 \hat{Q}|\phi_2\rangle \\ \vdots \\ \Gamma_1 \hat{P}|\Phi_1\rangle \\ \Gamma_2 \hat{P}|\Phi_2\rangle \\ \vdots \end{pmatrix} = E \begin{pmatrix} \gamma_1 \hat{Q}|\phi_1\rangle \\ \gamma_2 \hat{Q}|\phi_2\rangle \\ \vdots \\ \Gamma_1 \hat{P}|\Phi_1\rangle \\ \Gamma_2 \hat{P}|\Phi_2\rangle \\ \vdots \end{pmatrix}. \quad (15)$$

This yields a series of equations

$$\hat{H}_{QQ}\hat{Q}|\phi_j\rangle\gamma_j + \sum_{n=0}^N \hat{H}_{QP}\hat{P}|\Phi_n\rangle\Gamma_n = E\hat{Q}|\phi_j\rangle\gamma_j, \quad (16)$$

for  $j = 1, 2, \dots, M$  and

$$\hat{H}_{PP}\hat{P}|\Phi_n\rangle\Gamma_n + \sum_j H_{PQ}\hat{Q}|\phi_j\rangle\gamma_j = E\hat{P}|\Phi_n\rangle\Gamma_n \quad (17)$$

for  $n = 1, 2, \dots, N$ . The condition for Hermiticity of the Hamiltonian,  $\langle\Psi_\beta|\hat{H}|\Psi_\alpha\rangle = \langle\Psi_\alpha|\hat{H}|\Psi_\beta\rangle^*$ , allows us to determine that the value of the coupling constant,  $C$ , is  $C = \frac{4\hbar i}{2m}$  (see Appendix A).

### 3 The Reaction Matrix

We now have enough information to derive the reaction matrix for this system.

Let us first multiply Eq. (16) by  $\langle\phi_j|\hat{Q}$  to obtain

$$\langle\phi_j|\hat{H}_{QQ}|\phi_j\rangle\gamma_j + \sum_{n=1}^N \langle\phi_j|\hat{H}_{QP}|\Phi_n\rangle\Gamma_n = E\langle\phi_j|\hat{Q}|\phi_j\rangle\gamma_j \quad (18)$$

which reduces to

$$(\lambda_j - E)\gamma_j + C \frac{\hbar}{4i} \sum_{n=1}^N \phi_{j,n}^*(0) \frac{d\chi_n}{dx} \Big|_0 \Gamma_n = 0. \quad (19)$$

If we use Eq. (67) for the coupling constant,  $C$ , we can rewrite Eq. (19) and obtain the following expression for  $\gamma_j$ ,

$$\gamma_j = \frac{\hbar^2}{2m} \frac{1}{(E - \lambda_j)} \sum_{n=1}^N \phi_{j,n}^*(0) \frac{d\chi_n}{dx} \Big|_a \Gamma_n. \quad (20)$$

The continuity equation (65), when applied to energy eigenstates, yields

$$\Gamma_n \chi_n(0) = \sum_{j=1}^M \gamma_j \phi_{j,n}(0) = \sum_{n'=1}^N R_{n,n'} \frac{d\chi_{n'}}{dx} \Big|_0 \Gamma_{n'}. \quad (21)$$

where

$$R_{n,n'} = \frac{\hbar^2}{2m} \sum_{j=1}^M \frac{\phi_{j,n'}^*(0) \phi_{j,n}(0)}{(E - \lambda_j)} \quad (22)$$

is the  $(n, n')$ <sup>th</sup> matrix element of the reaction matrix.

We must now distinguish between propagating and evanescent modes. The states in the leads, for propagating modes, can be written

$$\Gamma_n \chi_n(x) = \frac{a_n}{\sqrt{k_n}} e^{-ik_n x} + \frac{b_n}{\sqrt{k_n}} e^{ik_n x}, \quad (23)$$

where

$$k_n = \sqrt{\frac{2mE}{\hbar^2} - \left(\frac{n\pi}{d+a}\right)^2} \quad (24)$$

If there are  $\nu$  propagating modes then  $n = 1, 2, \dots, \nu$ . Here we use a unit current normalization. The evanescent modes in the leads can be written

$$\Gamma_n \chi_n(x) = \frac{c_n}{\sqrt{k_n}} e^{-\kappa_n |x|}, \quad (25)$$

where

$$\kappa_n = \sqrt{\left(\frac{n\pi}{d+a}\right)^2 - \frac{2mE}{\hbar^2}} \quad (26)$$

For evanescent modes the index  $n = \nu + 1, \nu + 2, \dots, N$  where  $N \rightarrow \infty$ .

## 4 The Scattering Matrix

To obtain the scattering matrix, we must first separate the propagating modes from the evanescent modes. This first step is accomplished as follows. Using Eq. (23) and Eq. (25) we can write Eq. (21) in the matrix form

$$\begin{pmatrix} \bar{a} + \bar{b} \\ \bar{c} \end{pmatrix} = \begin{pmatrix} \bar{K}_p & 0 \\ 0 & \bar{K}_e \end{pmatrix} \begin{pmatrix} \bar{R}_{pp} & \bar{R}_{pe} \\ \bar{R}_{ep} & \bar{R}_{ee} \end{pmatrix} \begin{pmatrix} \bar{K}_p & 0 \\ 0 & \bar{K}_e \end{pmatrix} \begin{pmatrix} i(\bar{b} - \bar{a}) \\ \bar{c} \end{pmatrix}, \quad (27)$$

where

$$\bar{a} = \begin{pmatrix} a_1 \\ \vdots \\ a_\nu \end{pmatrix}, \quad \bar{b} = \begin{pmatrix} b_1 \\ \vdots \\ b_\nu \end{pmatrix}, \quad \bar{c} = \begin{pmatrix} c_{\nu+1} \\ \vdots \\ c_N \end{pmatrix},$$

$$\bar{K}_p = \begin{pmatrix} \sqrt{k_1} & \dots & 0 \\ \vdots & \ddots & \vdots \\ 0 & \dots & \sqrt{k_\nu} \end{pmatrix}, \quad \bar{K}_e = \begin{pmatrix} \sqrt{\kappa_1} & \dots & 0 \\ \vdots & \ddots & \vdots \\ 0 & \dots & \sqrt{\kappa_{N-\nu}} \end{pmatrix}$$

$$\begin{aligned} \bar{R}_{pp} &= \begin{pmatrix} R_{1,1} & \cdots & R_{1,\nu} \\ \vdots & \cdots & \vdots \\ R_{\nu,1} & \cdots & R_{\nu,\nu} \end{pmatrix}, & \bar{R}_{pe} &= \begin{pmatrix} R_{1,\nu+1} & \cdots & R_{1,N} \\ \vdots & \cdots & \vdots \\ R_{\nu,\nu+1} & \cdots & R_{\nu,N} \end{pmatrix}, \\ \bar{R}_{ep} &= \begin{pmatrix} R_{\nu+1,1} & \cdots & R_{\nu+1,\nu} \\ \vdots & \cdots & \vdots \\ R_{N,1} & \cdots & R_{N,\nu} \end{pmatrix}, & \bar{R}_{ee} &= \begin{pmatrix} R_{\nu+1,\nu+1} & \cdots & R_{\nu+1,N} \\ \vdots & \cdots & \vdots \\ R_{N,\nu+1} & \cdots & R_{N,N} \end{pmatrix} \end{aligned} \quad (28)$$

If we expand out Eq. (27), we find

$$\bar{a} + \bar{b} = i\bar{K}_p\bar{R}_{pp}\bar{K}_p(\bar{b} - \bar{a}) + \bar{K}_p\bar{R}_{pe}\bar{K}_e\bar{c} \quad (29)$$

$$\bar{c} = i\bar{K}_e\bar{R}_{ep}\bar{K}_p(\bar{b} - \bar{a}) + \bar{K}_e\bar{R}_{ee}\bar{K}_e\bar{c}. \quad (30)$$

From Eq. (30) we can write  $\bar{c}$  as

$$\bar{c} = \frac{i}{(\bar{1}_e - \bar{K}_e\bar{R}_{ee}\bar{K}_e)}\bar{K}_e\bar{R}_{ep}\bar{K}_p(\bar{b} - \bar{a}), \quad (31)$$

where  $\bar{1}_e$  is a unit matrix with the same dimensions as  $\bar{R}_{ee}$ . If we substitute Eq. (31) into Eq. (29), we find

$$\bar{a} + \bar{b} = i\bar{D}(\bar{b} - \bar{a}), \quad (32)$$

where

$$\bar{D} = \left[ \bar{K}_p\bar{R}_{pp}\bar{K}_p + \bar{K}_p\bar{R}_{pe}\bar{K}_e \frac{1}{(\bar{1}_e - \bar{K}_e\bar{R}_{ee}\bar{K}_e)} \bar{K}_e\bar{R}_{ep}\bar{K}_p \right]. \quad (33)$$

The second term on the right in Eq. (33) contains the effect of the evanescent states on the propagating modes in the waveguide. The *scattering matrix*,  $\bar{S}$ , relates the outgoing propagating modes to the incoming propagating modes through the relation,  $\bar{a} = \bar{S}\bar{b}$ . The scattering matrix is thus given by

$$\bar{S} = -\frac{(\bar{1}_p - i\bar{D})}{(\bar{1}_p + i\bar{D})}, \quad (34)$$

where  $\bar{1}_p$  is a unit matrix with the same dimension as  $\bar{R}_{pp}$ . We see from Eqs. (33) and (34), that the evanescent modes may play an important role in the scattering process. To see this effect on the resonance structure of  $\bar{S}$  matrix, we

obtain a more explicit form as follows. First we define the coupling matrices,

$$\bar{w}_{Np} \equiv \begin{pmatrix} \phi_{11} & \dots & \phi_{1p} \\ \vdots & & \vdots \\ \phi_{N1} & \dots & \phi_{Np} \end{pmatrix} \bar{K}_p \quad \text{and} \quad \bar{w}_{Ne} \equiv \begin{pmatrix} \phi_{11} & \dots & \phi_{1e} \\ \vdots & & \vdots \\ \phi_{N1} & \dots & \phi_{Ne} \end{pmatrix} \bar{K}_e, \quad (35)$$

where  $p$  is the number of propagating modes and  $e$  is the number of evanescent modes in the lead. The matrix  $\bar{D}$  can be written in terms of the coupling matrices as,

$$\begin{aligned} \bar{D} &= \bar{w}_{pN}^\dagger \frac{1}{E\bar{1}_N - \bar{H}_{in}} \bar{w}_{Np} \\ &+ \bar{w}_{pN}^\dagger \frac{1}{E\bar{1}_N - \bar{H}_{in}} \bar{w}_{Ne} \frac{1}{\bar{1}_e - \bar{w}_{eN}^\dagger \frac{1}{E\bar{1}_N - \bar{H}_{in}} \bar{w}_{Ne}} \bar{w}_{eN}^\dagger \frac{1}{E\bar{1}_N - \bar{H}_{in}} \bar{w}_{Np} \end{aligned} \quad (36)$$

where  $\bar{H}_{in}$  is a diagonal matrix formed by the eigenvalues of the Hamiltonian,  $H_{QQ}$ , inside the cavity. The second part of Eq. (36) can be rearranged by expanding in a series and regrouping terms,

$$\begin{aligned} \bar{D} &= \bar{w}_{pN}^\dagger \frac{1}{E\bar{1}_N - \bar{H}_{in}} \bar{w}_{Np} \\ &+ \bar{w}_{pN}^\dagger \frac{1}{E\bar{1}_N - \bar{H}_{in}} \bar{w}_{Ne} \bar{w}_{eN}^\dagger \frac{1}{E\bar{1}_N - \bar{H}_{in} - \bar{w}_{Ne} \bar{w}_{eN}^\dagger} \bar{w}_{Np}. \end{aligned}$$

This expression for  $\bar{D}$  can then be substituted into Eq. (34) and we obtain the following form for the scattering matrix,

$$\bar{S} = -(1 - 2i\bar{w}_{pN}^\dagger \frac{1}{E\bar{1}_N - \bar{H}_{in} - \bar{w}_{Ne} \bar{w}_{eN}^\dagger + i\bar{w}_{Np} \bar{w}_{pN}^\dagger} \bar{w}_{Np}) \quad (37)$$

As can be seen from the denominator of this expression, evanescent modes affect the positions of resonance poles in complex energy plane because of their dependence on both coupling matrices,  $\bar{w}_{pN}$  and  $\bar{w}_{eN}$ . Contributions from term,  $\bar{w}_{Ne} \bar{w}_{eN}^\dagger$  are not included in RRMT calculations. Also, the energy dependence of the coupling matrix,  $\bar{w}_{pN}$  is neglected in RRMT calculations, although this is known to various authors and they simply assume that the energy regions they consider are far from channel openings. As we see in Eq. (37), evanescent modes may play an important role in the scattering process, and in subsequent sections, we will investigate their effect on scattering of an electron from the ripple cavity.

## 5 Basis States for the Cavity Region

We now describe a method to obtain the complete set of eigenstates,  $\hat{Q}|\phi_j\rangle$ , of the Hamiltonian,  $H_{QQ}$ . We will require that these states have zero slope at the at the cavity-lead interface ( $x = 0$ ). We introduce a coordinate transformation which straightens the rippled wall of the cavity [9], [30]. Then we can obtain a Hamiltonian matrix which can be diagonalized to find the eigenvalues,  $\lambda_j$ , and eigenstates,  $\phi_j(x, y)$ . The first step is to write the eigenvalue equation,  $H_{QQ}\hat{Q}|\phi_j\rangle = \lambda_j\hat{Q}|\phi_j\rangle$  in configuration space. It takes the form

$$\frac{-\hbar^2}{2m} \left( \frac{d^2}{dx^2} + \frac{d^2}{dy^2} + V(x, y) \right) \phi_j(x, y) = \lambda_j \phi_j(x, y), \quad (38)$$

where  $\phi_j(x, y) \equiv \langle x, y | \hat{Q}|\phi_j\rangle$ . After the coordinate change,

$$u = x, \quad v = \frac{y}{d + a \cos(\frac{4\pi}{L}x)}, \quad (39)$$

we obtain an eigenvalue equation in terms of the coordinates,  $u$  and  $v$ , given by

$$\bar{H}\psi_j(u, v) \equiv -\frac{\hbar^2}{2m}(\partial_u^2 + h_1\partial_v^2 + h_2\partial_{uv}^2 + h_3\partial_v)\psi_j(u, v) = \lambda_j\psi_j(u, v) \quad (40)$$

where

$$h_1 = \frac{1 + v^2 g_u^2}{g^2}, h_2 = \frac{-2v g_u}{g}, h_3 = \frac{-v g_{uu}}{g} + \frac{2v g_u^2}{g^2},$$

$g = g(u) \equiv d + a \cdot \cos(\frac{4\pi}{L}u)$ ,  $g_u \equiv \frac{\partial g}{\partial u}$ , and  $\psi_j(u, v) = \phi_j(x(u, v), y(u, v))$ . The boundary conditions in  $(u, v)$  space are given by  $\partial_u \psi_l(0, v) = 0$ ,  $\psi_l(L, v) = 0$ ,  $\psi_l(u, 0) = 0$ , and  $\psi_l(u, 1) = 0$ , so that in terms of these coordinates the walls are straight. Note that in the  $(u, v)$  coordinate frame, the states,  $\psi_j(u, v)$  are normalized with a weighting factor,  $g(u)$ , so that

$$\iint g(u) \psi_j^\dagger(u, v) \psi_{j'}(u, v) du dv = \delta_{j, j'}, \quad (41)$$

The state,  $\psi_j(u, v)$ , can be expanded in terms of a Fourier basis,

$$\psi_j(u, v) = \sum_{m=1}^{\infty} \sum_{n=1}^{\infty} B_{mn}^j \phi_{mn}(u, v) \quad (42)$$

with

$$\phi_{mn}(u, v) = \frac{2}{\sqrt{L}} g^{-1/2} \sin(n\pi v) \cos\left(\frac{(2m-1)\pi u}{2L}\right), \quad (43)$$

where  $B_{mn}^j$  are the unknown expansion coefficients. As a result of this expansion, the boundary value problem is transformed into the eigenvalue problem,

$$\sum_{m=1}^{\infty} \sum_{n=1}^{\infty} H_{mnm'n'} B_{m'n'}^j = E_j B_{mn}^j. \quad (44)$$

The Hamiltonian matrix elements,  $H_{mnm'n'}$ , are given by

$$H_{mnm'n'} = \frac{4}{L} \int_0^L du \int_0^1 dv \sqrt{g} \sin(n\pi v) f \bar{H} (\sin(n'\pi v) f' / \sqrt{g}) \quad (45)$$

where  $f \equiv \cos\left(\frac{(2m-1)\pi u}{2L}\right)$ ,  $f' \equiv \cos\left(\frac{(2m'-1)\pi u}{2L}\right)$ ,  $g \equiv d + a \cos\left(\frac{4\pi u}{L}\right)$ , and  $\bar{H}$  is the differential operator defined in Eq. (40). Note that we cannot use integration by parts to get a symmetrical form, as was done in Refs. [9] and [30] because surface terms will not drop out.

We calculate the Hamiltonian matrix elements using Eq. (45). We reduce the double integral to a single integral after integrating in the  $v$  direction. After some algebra we find the following form which is suitable for numerical calculations,

$$\begin{aligned} H_{mnm'n'} = & -w_{mm'}^1 \delta_{nn'} / 2 + (n\pi)^2 w_{mm'}^2 \delta_{nn'} / 2 + (2(n\pi)^2 - 3) w_{mm'}^3 \delta_{nn'} \\ & + w_{mm'}^4 \delta_{nn'} / 4 + (1 - \delta_{nn'}) (-1)^{n+n'} \left( \frac{4w_{mm'}^3 n'^3 n}{(n^2 - n'^2)^2} + \frac{w_{mm'}^4 n n'}{(n^2 - n'^2)} \right) \end{aligned} \quad (46)$$

where

$$\begin{aligned} w_{mm'}^1 & \equiv \int_0^L du \frac{4f_{uu}g^2 - 4f_u g_u g - 2f g_{uu} g + 3f g_u^2}{4g^2} f' \\ w_{mm'}^2 & \equiv \int_0^L du \frac{f}{g^2} f', \quad w_{mm'}^3 \equiv \int_0^L du \frac{f g_u^2}{g^2} f' \\ w_{mm'}^4 & \equiv \int_0^L du \frac{-2f_u g_u g + f g_u^2 - f g_{uu} g + 2f g_u^2}{g^2} f' \end{aligned}$$

The eigenvalues and eigenvectors of  $\bar{H}$  can be calculated efficiently due to the sinusoidal integrals. Eigenvectors of  $\bar{H}$  give values for the expansion coefficients,

$B_{mn}^j$ , and the eigenfunctions in u-v space can be found from these coefficients. The solution can then be transformed back to x-y space to obtain the basis states,  $\phi_j(x, y)$ .

## 6 Accuracy of Reaction Matrix Theory Computations

We have computed the scattering matrix and the amplitude of the evanescent modes for the waveguide given by Fig. 1, using both the reaction matrix theory presented in the previous sections, and an independent finite element method (FEM) as a check on the reaction matrix results. For this comparison we used the following parameter values:  $a = 10\text{\AA}$ ,  $d = 100\text{\AA}$ ,  $L = 200\text{\AA}$ , and  $m = 0.067m_e$  where  $m_e$  is the free electron mass. This gives  $E_n = n^2 \frac{\hbar^2 \pi^2}{2m(d+a)^2} = (0.0622n^2)eV$  for the energy at which the  $n^{\text{th}}$  propagating mode appears.

We will discuss our results for the energy interval,  $E_1 < E < 9E_1$ , in which one propagating mode ( $E_1 < E < 4E_1$ ) and two propagating modes ( $4E_1 < E < 9E_1$ ) can exist in the leads. We studied both the case in which  $a = 0$ , so the cavity is rectangular, and the case  $a = 10\text{\AA}$  in which the dynamics in the cavity is fully chaotic [9]. We have computed the partial Wigner delay times,  $\tau_n = \hbar \frac{d\theta_n}{dE}$ , where  $\theta_n$  is the  $n^{\text{th}}$  eigenphase of the S-matrix.

For a rectangular cavity,  $a = 0$  (the upper boundaries of the rectangular region is shown with a dotted line in Fig.1), we can find analytic expressions for the S-matrix which serve as a check on the accuracy of our programs. For the energy regime where only one mode can propagate in the leads, the S-matrix (S-function in this case) is a complex number with unit magnitude and is given by the value of reflection coefficient,  $S = e^{i2kL}$ . This is the phase shift of the wave as it enters the cavity and reflects back to the entrance. The eigenphase of the S-matrix is  $\theta = 2kL$ . Since the phase angle depends linearly on  $k$ , no resonance occurs. The Wigner delay time has no peaks.

The reaction matrix for a rectangular cavity can be written exactly. Since

there is no mode coupling in the rectangular cavity, it is enough to calculate  $R_{11}$  in the energy regime where only one mode propagates. The eigenvalues of  $H_{QQ}$  take the form  $\frac{\hbar^2}{2m} \left( \frac{(m \cdot \pi)^2}{d^2} + \frac{((2 \cdot n - 1) \cdot \pi)^2}{(2 \cdot L)^2} \right)$ , where  $m$  and  $n$  positive integers representing the transverse and longitudinal degrees of freedom. We obtain

$$\begin{aligned} R_{11} &= \lim_{N \rightarrow \infty} \sum_{n=0}^N \frac{1}{e - (\pi/d)^2 - ((2 \cdot n - 1) \cdot \pi / (2L))^2} \\ &= \frac{\tan(L \cdot \sqrt{e - (\pi/d)^2})}{\sqrt{e - (\pi/d)^2}} = -\frac{\tan(kL)}{k}, \end{aligned} \quad (47)$$

where  $e = 2mE/\hbar^2$ . The S function is given in terms of  $R_{11}$ ,

$$S = -\frac{1 - ikR_{11}}{1 + ikR_{11}} = -\frac{1 + i \tan(kL)}{1 - i \tan(kL)} = e^{i2kL}, \quad (48)$$

so the eigenphase is given by  $\theta = 2kL$  which coincides with the exact result.

We can now check the accuracy of the methods we are using. In Fig. 2, the sum in Eq. (47) is truncated at  $N = 1000$  and  $N = 10000$  and used to compute the reflection coefficient. The relative error is less than  $10^{-4}$  for the number of terms we kept in following calculations. The phase angle curve calculated by FEM is in agreement to the order of  $10^{-5}$  with the exact result. More discussion about the FEM method can be found in ref [9] and references cited there.

Let us now consider the case of the ripple cavity. In Fig. 3, we show the Wigner delay times calculated by using Eq. (34) and we compare them to the Wigner delay times obtained from the FEM calculation. In Fig. 3(a) we show the Wigner delay time,  $\tau_1$ , in the energy interval where there is one propagating mode in the leads. In Fig. 3(b), we show two partial Wigner delay times,  $\tau_1$  and  $\tau_2$ , in the energy interval where there are 2 modes in the lead. We have kept up to 2500 terms in Eq. (22). We checked the accuracy of these eigenvalues by increasing the size of the Hamiltonian matrix and comparing eigenvalues of a matrix with 5500 eigenvalues, and a matrix with 10,000 eigenvalues. We found that the first 2500 eigenvalues were the same to an accuracy greater than  $10^{-5}$ . We used the first 2500 eigenvalues and their eigenstates to construct the reaction matrix.

We also looked at the analytic continuation of the S-matrix into the lower complex energy plane to see the resonances explicitly. In Fig. 4 we used Eq. (34) (including evanescent modes) to obtain the analytic continuation of the S-matrix. The position of the three peaks, shown in Fig. (4), are  $E_1 = 1.3585 - i0.123$ ,  $E_2 = 1.8991 - i0.2403$ , and  $E_3 = 3.1241 - i0.2316$ . The real part of peak position shows the resonance energy and the imaginary part shows its lifetime. These are both consistent with Fig. (3.a). The full width at half maximum of resonances in Fig. (3.a) is in agreement with imaginary parts of S-Matrix poles in Fig. (4). We obtained the following numerical values for the resonance positions,  $E_i$ , and their widths,  $\Gamma_i$  in Fig. (3.a), ( $E_1 = 1.3733$ ,  $\Gamma_1 = 0.16$ ), ( $E_2 = 1.8917$ :  $\Gamma_2 = 0.20$ ), and ( $E_3 = 3.1359$ ,  $\Gamma_3 = 0.21$ ), where  $\Gamma$  is defined as the full width at half maximum. In the upper half plane one gets corresponding zeros of the S-Matrix.

## 7 The Effect of Evanescent Modes

For the shape of waveguide cavity that we consider here, the effect of evanescent modes on Wigner delay times appears to be most important just before a new channel opens in the lead. We have studied the effect of evanescent modes using parameters,  $a = 10\text{\AA}$ ,  $d = 100\text{\AA}$ ,  $L = 500\text{\AA}$ , and  $m = 0.067m_e$ , and we use the form of the S-matrix in Eq. (34) to obtain our results. We compare the variation of S-matrix elements,  $S_{ij}$ , for an S-matrix which includes the evanescent modes ( $\bar{K}_e \neq 0$ ), with an S-matrix,  $\bar{S}^0$ , which excludes evanescent modes ( $\bar{K}_e = 0$ ). We use the cavity length,  $L = 500\text{\AA}$ , (rather than the smaller length  $L = 200\text{\AA}$  used to check accuracy) to increase the density of resonances in any given energy interval. In a mesh based numerical method (like FEM or a finite difference) increasing cavity length is numerically is not efficient due to the increasing number of nodal points, but the reaction matrix approach can easily accomodate longer cavities. In Fig. (5.a) we show the effect of the evanescent modes on the Wigner delay time at energies just below where

the second channel opens and, as we expect, there is a considerable increase in the delay of the electron. The absolute value of the amplitude,  $c_1$ , of the first evanescent mode also increases just before the second propagating channel opens as shown in Fig. (5.b). The effect of the first evanescent mode,  $c_1$ , is dominant since the amplitudes of the second and higher evanescent modes are near zero. A similar behavior of the evanescent modes occurs at energies just below where the third propagating channel opens. There again, one evanescent mode becomes dominant. In Figs. (5.c) and Fig. (5.d) we compare the behavior of first and second partial Wigner delay times,  $\tau_1$  and  $\tau_2$ , respectively, both for the case when the contributions of the evanescent modes are included and for the case when they are removed in calculations of the S-matrix in this energy regime.

In Fig. 6 we plot  $|S_{11}|$  and  $|S_{12}|$  in the energy interval,  $4E_1 < E < 9E_1$  (two propagating modes). We find that  $|S_{22}| = |S_{11}|$  and  $|S_{21}| = |S_{12}|$ . Therefore we show only these two matrix elements. In Fig. 7, we show the effect of evanescent modes on S-matrix elements in the two mode energy regime by plotting the differences,  $|S_{11}^0| - |S_{11}|$  and  $|S_{12}^0| - |S_{12}|$ . The difference in the magnitude of the S-matrix elements is small, but the difference in the slopes can be fairly large.

We have also looked at the analytic continuation of S-matrix elements in the complex energy plane and we find good agreement with the predictions of Wigner delay time plots. In Fig. 8, we show partial Wigner delay times in energy interval,  $4E_1 < E < 9E_1$ . In Fig. 9 we show the behavior of  $|S_{11}|$  in the complex energy plane. Fig. 9.a gives large scale behavior, and Fig. 9.b focuses on behavior near the real axis. The poles near to real energy axis (shown in Fig. 9.b) determine the sharp peaks in the Wigner delay times. The poles further from the real axis determine the broader peaks in the Wigner delay time plots.

In Fig. 10 and in Fig. 11 we show the effect of the energy dependence of the coupling matrices,  $\bar{w}_{Np}$  and  $\bar{w}_{Ne}$ . This energy dependence is always neglected

in RRMT calculations. In Fig. 10, we plot  $|S_{11}|$ , both for the case when the energy dependence of  $\bar{w}_{Np}$  and  $\bar{w}_{Ne}$  is taken into account (full line), and for the case when the energy dependence of  $\bar{w}_{Np}$  and  $\bar{w}_{Ne}$  is fix at value,  $E = 6.5E_1$  (dotted-dashed line). In Fig. 11, the effect of the energy dependence of  $\bar{w}_{Np}$  and  $\bar{w}_{Ne}$  on the distributions of poles in the complex energy plane is shown. The position of S-matrix poles changes when the variation with energy of the coupling constants is not included. In Fig. 11, the solid lines are contour lines of  $|S_{11}|$  for the reaction matrix calculation with evanescent modes included and the energy dependence of  $\bar{w}_{Np}$  and  $\bar{w}_{Ne}$  included as in Fig. (6). The dotted-dashed lines shows the same quantity but using coupling matrices,  $\bar{w}_{Np}$  and  $\bar{w}_{Ne}$ , with dependence on energy,  $E$  fixed at the real value  $E = 6.5E_1$ . Neglect of the energy dependence of the coupling constants causes a shift of the poles away from their true positions. This shift is small in the neighborhood of the fixed energy,  $E = 6.5E_1$ , but it grows as one moves further away in energy.

## 8 The Signatures of Chaos

In this section we compute the statistical properties of the Wigner delay times obtained for deterministic scattering of the electron from the ripple cavity. We consider only configurations of the ripple cavity for which the dynamics of the cavity is classically chaotic. One can use either Eq. (34) or Eq. (37) to calculate Wigner delay times deterministically. We have checked that they give identical answers. For the deterministic calculations, we can get sufficient data to develop good statistics by changing the ripple size from  $a = 10\text{\AA}$  to  $a = 30\text{\AA}$  in units of  $0.2\text{\AA}$ . In Figs. (9a), (9.b), and (9.c), we show the statistics for the total Wigner delay times for deterministic scattering for the cases when  $M = 2$ ,  $M = 6$ , and  $M = 16$  propagating modes, respectively, exist in the leads. In these Figures,  $P(\tau)$  is the histogram of Wigner delay times normalized so the area is equal to one, and  $\langle \tau \rangle$  is the mean Wigner delay time. The distribution,  $P(\tau)$ , shifts from a Poisson-like distribution to Gaussian-like distribution as we increase

the number of channels. For a small number of channels the distribution is asymmetric and has a long tail.

We also looked at the statistics of the total Wigner delay times obtained by replacing the S-matrix in Eq. (37), by the equation

$$\bar{S} = -(1 + 2ig^2\bar{w}^\dagger \frac{1}{E\bar{1}_N - \bar{H}'_{in} - ig^2\bar{w}\bar{w}^\dagger} \bar{w}), \quad (49)$$

where  $\bar{H}'_{in}$  is chosen from an Gaussian Orthogonal Ensemble (GOE) and the coupling matrix,  $\bar{w}$ , is constructed from M eigenvectors of the realizations of  $\bar{H}'_{in}$  in the same GOE ensemble. Note that  $g$  is a coupling constant that must be determined from experiment. We also checked our result by building  $\bar{w}$  using the M eigenvectors of each realization of  $\bar{H}_{in}$  and we get a similar distribution for the corresponding number of channels.

We have calculated the Wigner delay time by taking the derivative of the S-matrix eigenphase curve,  $\theta(E)$  versus  $E$ , in two different ways. The first way is to take two neighboring energy points (we chose  $E=0$  and  $E=0.001$ ) and used these obtain one Wigner delay time for each realization of  $H'_{in}$ . The second way is to obtain a whole series of Wigner delay times from the  $\theta(E)$  versus  $E$  curve for a single realization of  $H'_{in}$ . We have checked that these two methods give similar results as we would expect due to ergodicity.

In Fig. (12) we show the distribution of total Wigner delay times obtained from the Gaussian Orthogonal Ensemble as described above. The middle column with Figures Figs. (12.d), (12.e), and (12.f) corresponds to a coupling constant,  $g = 1.8$ , which is the strong coupling regime for RRMT. The right-most column with Figures Figs. (12.g), (12.h), and (12.i) corresponds to a coupling constant  $g = 1.0$ . The distribution of total Wigner delay times for our deterministic scattering from the chaotic ripple cavity, agrees qualitatively with the predictions of random matrix theory for strong coupling. This is consistent with the fact that the opening between the ripple cavity and the leads for our case is very large.

## 9 Conclusion

In this paper we have studied the effect that evanescent modes have on the scattering properties of an electron in a waveguide with a “chaotic” cavity. We have reformulated the reaction matrix theory of electron waveguide scattering to explicitly include the effect of evanescent modes. We have found that evanescent modes can increase the delay of the electron for energies near the opening of new channels. This effect has been seen before [25]. The scattering system we have considered is relatively “soft”. There are no impurities and no sharp corners to snag evanescent modes, and yet their effect is still noticeable. For systems with impurities and sharp corners, we expect the effect of evanescent modes to be even more dramatic.

We have also studied the effect of neglecting the energy dependence of the coupling matrices that appear in the reaction matrix approach to scattering. This appears to cause an effective repulsion on the positions of quasibound state poles.

The effects of both the evanescent modes and the energy dependence of coupling matrices are routinely neglected in RRMT, and this should be kept in mind when attempting to use that theory to make predictions about real waveguide scattering experiments or numerical simulation of deterministic waveguide scattering systems.

We have also studied the statistical distribution of the Wigner delay times for scattering from our chaotic waveguide cavity, for the case of  $M = 2$ ,  $M = 6$  and  $M = 16$  propagating modes. To build adequate statistics for comparison with RRMT predictions, we have included data for a range of ripple amplitudes, being careful to include data only from the regime where the internal dynamics of the ripple cavity is completely chaotic. If the ripple amplitude is too large or too small, the cavity will again develop a mixed phase space [30]. We find fairly good qualitative agreement with the predictions of strong coupling RRMT.

## 10 Acknowledgements

The authors wish to thank the Welch Foundation, Grant No.F-1051, NSF Grant INT-9602971 and DOE contract No.DE-FG03-94ER14405 for partial support of this work. We also thank the University of Texas at Austin High Performance Computing Center for use of their computer facilities, and we thank German Luna-Acosta and Thomas Seligman for helpful comments.

## References

- [1] E. P. Wigner *Conference on Neutron Physics by Time-of-flight* Gattingburg, Tennessee, November 1956, see Oak Ridge Natl. Lab. Rept. **ORNL-2309**
- [2] S. W. McDonald, A. N. Kaufman, Phys. Rev. Lett. **42** 1189 (1979)
- [3] R. Blumel and U. Smilansky, Phys. Rev. Lett. **64** 241 (1990)
- [4] Eyal Doron, U. Smilansky *Nonlinearity* **5** 1055 (1991).
- [5] H. U. Baranger, R. A. Jalabert, A. D. Stone *Chaos* **3** 665 (1993).
- [6] W. A. Lin and J.B. Delos, R. V. Jensen, *Chaos*(1993) vol.3(4) p.655-664
- [7] Pierre Gaspard and Stuart A. Rice, J. Chem. Phys. **90** 2225 (1989)
- [8] C. Rouivenez and U. Smilansky, J. Phys. A. **28** 77 (1995)
- [9] Gursoy B. Akguc and L.E. Reichl, J. Stat. Phys. **98** 813 (2000).
- [10] E.P. Wigner and L.E. Eisenbud, Phys. Rev. **72** 29 (1949).
- [11] A.M. Lane and R.G. Thomas, Rev. Mod. Phys. **30** 257 (1958).
- [12] C. Bloch, Nuclear Physics **4** 503 (1957).
- [13] H. Feshbach, Ann. Phys. **19** 287 (1962).
- [14] B.S. Pavlov, Theor. Math. Phys. **59** 544 (1984); Russ. Math. Surveys **42** 127 (1987).
- [15] Charles E. Porter, Norbert Rosenweig, Physica A **44** (1960), See also, Charles E. Porter *Statistical Theories of Spectra: Fluctuations* Academic Press, Newyork (1960)
- [16] C.M. Marcus, and R.M. Westervelt, P.f. Hopkins, and A.C. Gossard *Chaos* **3** 643 (1993).

- [17] H.-J. Stockman and J. Stein, Phys. Rev. Lett. **64** 2215(1990)
- [18] E. Wigner, Phys. Rev. **73** 1002(1948)
- [19] W. Meyerhof, Phys. Rev. **129** 692(1963)
- [20] F. Barker, P. Treacy, Nucl. Phys. **38** 33(1962)
- [21] D. Inglis, Nucl. Phys. **30** 1 (1962)
- [22] C.H. Lewenkopf and H.A. Weidenmuller, Annals of Physics **212** 53 (1991).
- [23] Y.V. Fyodorov and H-J Sommers, J. Math. Phys. **38** 1918 (1997).
- [24] S. Albeverio, F. Haake, P. Kurasov, M. Kus, P. Seba, J. Math. Phys. **37** 4888 (1996).
- [25] Daniel Boese, Markus Lischka, L.E. Reichl, Phys. Rev. B **61** 5632 (2000).
- [26] Kyungsun Na and L.E. Reichl, J. Stat. Phys. **92** 519 (1998); Phys. Rev. B **59** 13073 (1999).
- [27] Suhan Ree and L.E. Reichl, Phys. Rev. B **59** 8163 (1999).
- [28] I.S. Gradshteyn and I.M. Ryzhik, *Table of Integrals, Series, and Products*, (Academic press, New York, 1980), no.1.421.
- [29] D. Bohm, *Quantum Theory* (Prentice-Hall, Inc. Englewood Cliffs, N.J., 1950), p. 260; E.P. Wigner, Phys. Rev. **98** 145 (1955); F.T. Smith, Phys. Rev. **118** 349 (1960).
- [30] G.A. Luna-Acosta, Kyungsun Na, L.E. Reichl, and A. Krokhin, Phys. Rev. E (1996) **53** 3271 (1996).

## 11 Appendix A: Hermiticity Condition

Consider the arbitrary states,  $|\Psi_\alpha\rangle$  and  $|\Psi_\beta\rangle$ . The condition for Hermiticity of these states is that

$$\langle\Psi_\beta|\hat{H}|\Psi_\alpha\rangle - \langle\Psi_\alpha|\hat{H}|\Psi_\beta\rangle^* = 0. \quad (50)$$

We will use this condition to determine the coupling constant  $C$  (this method of determining the strength of the coupling was first suggested by Pavlov [14]). We can decompose the states  $|\Psi_\alpha\rangle$  and  $|\Psi_\beta\rangle$  into their contributions to the two disjoint configuration space regions and write them in the form,

$$|\Psi_\alpha\rangle = \hat{Q}|\Psi_\alpha\rangle + \hat{P}|\Psi_\alpha\rangle = \sum_{j=1}^M a_j \hat{Q}|\phi_j\rangle + \sum_{n=1}^N A_n \hat{P}|\Phi_n\rangle, \quad (51)$$

where  $a_j = \langle\phi_j|\hat{Q}|\Psi_\alpha\rangle$  and  $A_n = \langle\Phi_n|\hat{P}|\Psi_\alpha\rangle$ , and

$$|\Psi_\beta\rangle = \hat{Q}|\Psi_\beta\rangle + \hat{P}|\Psi_\beta\rangle = \sum_{j=1}^M b_j \hat{Q}|\phi_j\rangle + \sum_{n=1}^N B_n \hat{P}|\Phi_n\rangle, \quad (52)$$

where  $b_j = \langle\phi_j|\hat{Q}|\Psi_\beta\rangle$  and  $B_n = \langle\Phi_n|\hat{P}|\Psi_\beta\rangle$ . Inside the cavity,  $0 \leq x < L$ , we have expanded  $|\Psi_\alpha\rangle$  and  $|\Psi_\beta\rangle$  in terms of the complete set of energy eigenstates,  $\hat{Q}|\phi_j\rangle$ , of the Hamiltonian,  $\hat{H}_{QQ}$ . In the lead,  $-\infty \leq x < 0$ , we have expanded  $|\Psi_\alpha\rangle$  and  $|\Psi_\beta\rangle$  in terms of the complete set of energy eigenstates,  $\hat{P}|\Phi_n\rangle$ , of the Hamiltonian,  $\hat{H}_{PP}$ .

The Hermiticity condition takes the form

$$\begin{aligned} & \langle\Psi_\beta|\hat{H}|\Psi_\alpha\rangle - \langle\Psi_\alpha|\hat{H}|\Psi_\beta\rangle^* \\ &= \sum_{j=1}^M [\langle\phi_j|\hat{H}_{QQ}|\phi_j\rangle - \langle\phi_j|\hat{H}_{QQ}|\phi_j\rangle^*] a_j b_j^* \\ & \quad + \sum_{j=1}^M \sum_{n=1}^N [\langle\phi_j|\hat{H}_{QP}|\Phi_n\rangle - \langle\Phi_n|\hat{H}_{PQ}|\phi_j\rangle^*] a_j^* B_n \\ & \quad + \sum_{j=1}^M \sum_{n=1}^N [\langle\Phi_n|\hat{H}_{PQ}|\phi_j\rangle - \langle\phi_j|\hat{H}_{QP}|\Phi_n\rangle^*] b_j A_n^* \\ & \quad + \sum_{n=1}^N [\langle\Phi_n|\hat{H}_{PP}|\Phi_n\rangle - \langle\Phi_n|\hat{H}_{PP}|\Phi_n\rangle^*] A_n^* B_n = 0. \end{aligned} \quad (53)$$

We can now evaluate Eq. (53) term by term. The Hamiltonian,  $\hat{H}_{QQ}$ , is Hermitian and its eigenvalues are real so we immediately have  $\langle \phi_j | \hat{H}_{QQ} | \phi_j \rangle - \langle \phi_j | \hat{H}_{QQ} | \phi_j \rangle^* = \lambda_j - \lambda_j^* = 0$ . We will assume boundary conditions  $\frac{d\phi_j}{dx}|_{x=a} = 0$  and use Eqs. (9) and (10). Then *for these special boundary conditions* we find  $\langle \Phi_n | \hat{H}_{PQ} | \phi_j \rangle = 0$  and  $\langle \Phi_n | \hat{H}_{PQ} | \phi_j \rangle^* = 0$ . Thus, the Hermiticity condition reduces to

$$\begin{aligned} & \langle \Psi_\beta | \hat{H} | \Psi_\alpha \rangle - \langle \Psi_\alpha | \hat{H} | \Psi_\beta \rangle^* \\ &= \sum_{j=1}^M \sum_{n=1}^N [\langle \phi_j | \hat{H}_{QP} | \Phi_n \rangle a_j^* B_n - \langle \phi_j | \hat{H}_{QP} | \Phi_n \rangle^* b_j A_n^*] \\ &+ \sum_{n=1}^N [\langle \Phi_n | \hat{H}_{PP} | \Phi_n \rangle - \langle \Phi_n | \hat{H}_{PP} | \Phi_n \rangle^*] A_n^* B_n = 0. \end{aligned} \quad (54)$$

It is useful now to perform the spatial integrations implicit in Eq. (54). Let us first consider the last term. We can write  $\Phi_n(x, y) \equiv \langle x, y | \Phi_n \rangle = \chi_n(x) \sqrt{\frac{2}{d+a}} \sin\left(\frac{n\pi y}{d+a}\right)$ . If we substitute into the last term in Eq. (54) and perform the integration over  $y$ , we obtain

$$\begin{aligned} & \langle \Phi_n | \hat{H}_{PP} | \Phi_n \rangle - \langle \Phi_n | \hat{H}_{PP} | \Phi_n \rangle^* \\ &= \frac{-\hbar^2}{2m} \int_{-\infty}^0 dx \left[ \chi_n^*(x) \frac{d^2}{dx^2} \chi_n(x) - \chi_n(x) \frac{d^2}{dx^2} \chi_n^*(x) \right] \\ &= \frac{-\hbar^2}{2m} \left[ \chi_n^*(x) \frac{d}{dx} \chi_n(x) - \chi_n(x) \frac{d}{dx} \chi_n^*(x) \right]_{-\infty}^0. \end{aligned} \quad (55)$$

Note also that

$$\begin{aligned} \langle \phi_j | \hat{H}_{QP} | \Phi_n \rangle &= C \frac{\hbar}{i} \int_0^L dx_1 \int_0^{g(x_1)} dy_1 \int_{-\infty}^0 dx_0 \int_0^{d+a} dy_0 \\ &\times \langle \phi_j | x_1, y_1 \rangle \delta(x_1) \delta(x_1 - x_0) \delta(y_1 - y_0) \frac{d}{dx_0} \langle x_0, y_0 | \Phi_n \rangle. \end{aligned} \quad (56)$$

Perform the integration over  $x_1$  and notice that  $g(0) = d + a$ . Then Eq. (56) takes the form

$$\begin{aligned} \langle \phi_j | \hat{H}_{QP} | \Phi_n \rangle &= C \frac{\hbar}{2i} \int_0^{d+a} dy_1 \int_{-\infty}^0 dx_0 \int_0^{d+a} dy_0 \\ &\times \langle \phi_j | 0, y_1 \rangle \delta(x_0) \delta(y_1 - y_0) \frac{d}{dx_0} \langle x_0, y_0 | \Phi_n \rangle. \end{aligned} \quad (57)$$

The cavity basis states, *at the interface*, can be written

$$\langle \phi_j | 0, y \rangle = \phi_{j,n}^*(0) \sqrt{\frac{2}{d+a}} \sin\left(\frac{n\pi y}{d+a}\right). \quad (58)$$

Thus if we perform the remaining integrations in Eq. (57), we finally obtain

$$\langle \phi_j | \hat{H}_{QP} | \Phi_n \rangle = C \frac{\hbar}{4i} \phi_{j,n}^*(0) \frac{d\Phi_n}{dx} \Big|_0. \quad (59)$$

We can now combine the above results and write the Hermiticity condition in the form

$$\begin{aligned} & C \frac{\hbar}{4i} \sum_{j=1}^M \sum_{n=1}^N \left( \phi_{j,n}^*(0) \frac{d\chi_n}{dx} \Big|_0 a_j^* B_n - \phi_{j,n}(0) \frac{d\chi_n^*}{dx} \Big|_0 b_j A_n^* \right) \\ & + \frac{-\hbar^2}{2m} \sum_{n=1}^N \left[ \chi_n^*(x) \frac{d}{dx} \chi_n(x) - \chi_n(x) \frac{d}{dx} \chi_n^*(x) \right]_{-\infty}^0 A_n^* B_n = 0 \end{aligned} \quad (60)$$

for the case of zero-slope boundary conditions for the cavity basis states. The boundary conditions at  $x = -\infty$  cannot depend on details of the interface at  $x = 0$ . Therefore we must satisfy the conditions,

$$\begin{aligned} & C \frac{\hbar}{4i} \sum_{j=1}^M \sum_{n=1}^N \left( \phi_{j,n}^*(0) \frac{d\chi_n}{dx} \Big|_0 a_j^* B_n - \phi_{j,n}(0) \frac{d\chi_n^*}{dx} \Big|_0 b_j A_n^* \right) \\ & + \frac{-\hbar^2}{2m} \sum_{n=1}^N \left[ \chi_n^*(x) \frac{d}{dx} \chi_n(x) - \chi_n(x) \frac{d}{dx} \chi_n^*(x) \right]_{x=0} A_n^* B_n = 0 \end{aligned} \quad (61)$$

and

$$\frac{-\hbar^2}{2m} \sum_{n=1}^N \left[ \chi_n^*(x) \frac{d}{dx} \chi_n(x) - \chi_n(x) \frac{d}{dx} \chi_n^*(x) \right]_{x=-\infty} A_n^* B_n = 0, \quad (62)$$

separately. The Hermiticity condition, Eq. (61), is very simply satisfied if we let

$$C \frac{\hbar}{4i} \sum_{j=1}^M \phi_{j,n}^*(0) a_j^* = \frac{\hbar^2}{2m} \chi_n^*(0) A_n^* \quad (63)$$

and

$$C \frac{\hbar}{4i} \sum_{j=1}^M \phi_{j,n}(0) b_j = \frac{\hbar^2}{2m} \chi_n(0) B_n \quad (64)$$

These relations will be useful in the next section.

We now have enough information that we can determine the value of the coupling constant,  $C$ . Any state in the waveguide must satisfy the condition that it be a continuous function of  $x$  and  $y$ , and that its slope be a continuous function of  $x$  and  $y$ . Let us consider the state,  $|\Psi_\beta\rangle$ . We require that

$$\langle 0, y | \hat{Q} | \Psi_\beta \rangle = \langle 0, y | \hat{P} | \Psi_\beta \rangle. \quad (65)$$

This, in turn, implies that

$$\sum_{j=1}^M \phi_{j,n}(0) b_j = \chi_n(0) B_n. \quad (66)$$

If we now compare Eqs. (64) and (66), we find that the coupling constant is given by

$$C = \frac{4\hbar i}{2m}. \quad (67)$$

In Section (4), we use these results to make contact with scattering theory.

Figure 1: The geometry of the two dimensional electron wave guide used in our calculations. The rippled waveguide is the region defined with solid lines, rectangular waveguide is the region whose upper boundary is given by the dotted line. The dotted-dashed line shows the interference between leads and scattering region. Here ‘a’ is the width of the ripple, ‘d’ is the width of the rectangular waveguide, scattering cavity extends from  $x = 0$  to  $x = L$

Figure 2: Error in eigenphase,  $\theta$ , versus energy for an R-Matrix with  $N = 1000$  and  $N = 10000$  terms kept in the sum and the FEM calculation of  $\theta$ . The errors are calculated in terms of the fractional deviation of the numerically computed eigenphase,  $\theta_c$ , from the exact eigenphase  $\theta_e = 2kL$ .

Figure 3: (a) Wigner delay time,  $\tau_1$ , for rippled waveguide with parameters,  $a = 10\text{\AA}$ ,  $d = 100\text{\AA}$ ,  $L = 200\text{\AA}$ , for the energies such that only one propagating mode exists in the lead. The dashed line is for reaction matrix calculations, the solid line is from finite element calculations. (b) Partial Wigner delay times,  $\tau_1$  and  $\tau_2$ , when there are two propagating modes in the leads. The dashed lines are the reaction matrix results and the solid lines are the finite element results.

Figure 4: Poles of the S-matrix in the lower complex energy plane for an energy interval with only one propagating mode in the lead, obtained from Eq. (34). The waveguide parameters are  $a = 10\text{\AA}$ ,  $d = 100\text{\AA}$ ,  $L = 200\text{\AA}$ .

Figure 5: The effect of evanescent modes for a waveguide with parameters  $a = 10\text{\AA}$ ,  $d = 100\text{\AA}$ ,  $L = 500\text{\AA}$ . (a) The solid line is Wigner delay time,  $\tau_1$ , in the one channel regime,  $E_1 < E < 4E_1$ , for an energy interval just before a second propagating channel opens in the lead. The dashed line shows  $\tau_1$  when no evanescent modes are included in calculations. (b) The amplitudes,  $c_1$  and  $c_2$ , of the first two evanescent modes in the same energy interval as in (a). (c) The solid line shows the first partial Wigner delay time,  $\tau_1$  just before the opening of the third channel. The dashed line is for the case when no evanescent modes are included in calculating  $\tau_1$ . (d) The same as (c) for the second partial Wigner delay time,  $\tau_2$ .

Figure 6: The absolute value of S-matrix elements,  $|S_{11}|$  and  $|S_{12}|$ , in two modes energy interval,  $4E_1 < E < 9E_1$ , where two propagating channels are allowed. The waveguide parameters are  $a = 10\text{\AA}$ ,  $d = 100\text{\AA}$ ,  $L = 500\text{\AA}$ .

Figure 7: Wigner delay times for the energy interval,  $4E_1 < E < 9E_1$ , where two propagating channels are allowed. The waveguide parameters are  $a = 10\text{\AA}$ ,  $d = 100\text{\AA}$ ,  $L = 500\text{\AA}$ .

Figure 8: Poles of  $|S_{11}|$  in the lower complex energy plane for the energy interval,  $4E_1 < \text{Re}(E) < 9E_1$ . The waveguide parameters are  $a = 10\text{\AA}$ ,  $d = 100\text{\AA}$ ,  $L = 500\text{\AA}$ . (a)  $|S_{11}|$  for  $0 < \text{Im}(E) < -0.95E_1$ . (Only points for which  $|S_{11}| < 200$  are shown.) (b)  $|S_{11}|$  for  $0 < \text{Im}(E) < -0.075E_1$ .

Figure 9: The difference between S-matrix element,  $|S_{11}|$  with evanescent modes, and S-matrix element,  $|S_{11}^0|$  without evanescent modes. The waveguide parameters are  $a = 10\text{\AA}$ ,  $d = 100\text{\AA}$ ,  $L = 500\text{\AA}$ .

Figure 10: The value of  $|S_{11}|$ , when we include the energy dependence of the coupling matrices  $\bar{w}_{Np}$  and  $\bar{w}_{Ne}$  (solid line), and its value,  $|S_{11}^{noen}|$ , when we fix the energy dependence of the coupling matrices  $\bar{w}_{Np}$  and  $\bar{w}_{Ne}$  to be  $E = 6.5E_1$  (dotted-dashed line). The cavity parameters The waveguide parameters are  $a = 10\text{\AA}$ ,  $d = 100\text{\AA}$ ,  $L = 500\text{\AA}$ .

Figure 11: The value of  $|S_{11}|$ , in the complex energy plane, when we take into account the energy dependence of the coupling matrices  $\bar{w}_{Np}$  and  $\bar{w}_{Ne}$  (solid line), and its value,  $|S_{11}^{noen}|$ , when we fix the energy dependence of the coupling matrices  $\bar{w}_{Np}$  and  $\bar{w}_{Ne}$  to be  $E = 6.5E_1$  (dotted-dashed line). The cavity parameters  $a = 10\text{\AA}$ ,  $d = 100\text{\AA}$ ,  $L = 500\text{\AA}$ . (Only points for which  $|S_{11}| < 200$  are shown.)

Figure 12: Histograms of Wigner delay times for different numbers of propagating channels,  $M$  for the case of deterministic scattering ((a)-(c)) and RRMT predictions, (d)-(i). (a) Deterministic scattering with  $M = 2$  for  $a = 10\text{\AA}$ ,  $d = 100\text{\AA}$ ,  $L = 500\text{\AA}$ . (b) Same as (a) for  $M = 6$ . (c) Same as (a) for  $M = 16$ . (d)  $M = 2$  RRMT result with coupling constant,  $g = 1.8$ . (e) Same as (d) for  $M = 6$ . (f) Same as (d) for  $M = 16$ . (g)  $M = 2$  RRMT result with a unit coupling constant  $g = 1$ . (h) Same as (g) for  $M = 6$ . (i) Same as (g) for  $M = 16$ .

Fig.1, G.B. Akguc and L.E.Reichl

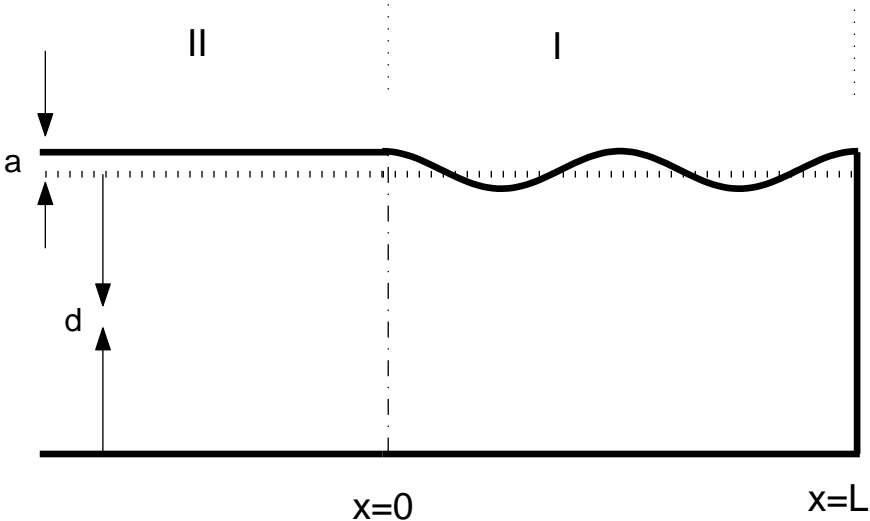


Fig.2, G.B. Akguc and L.E.Reichl

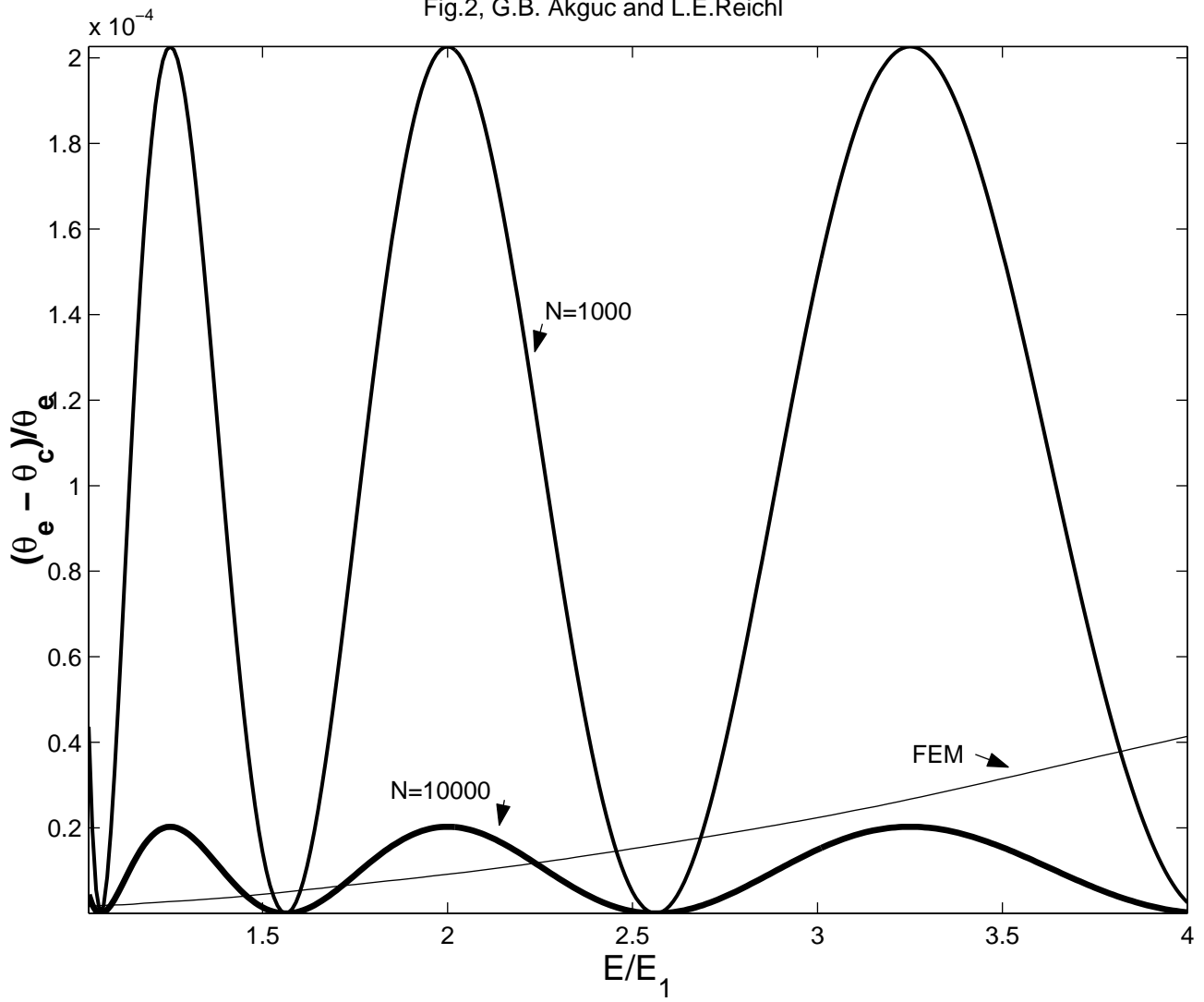
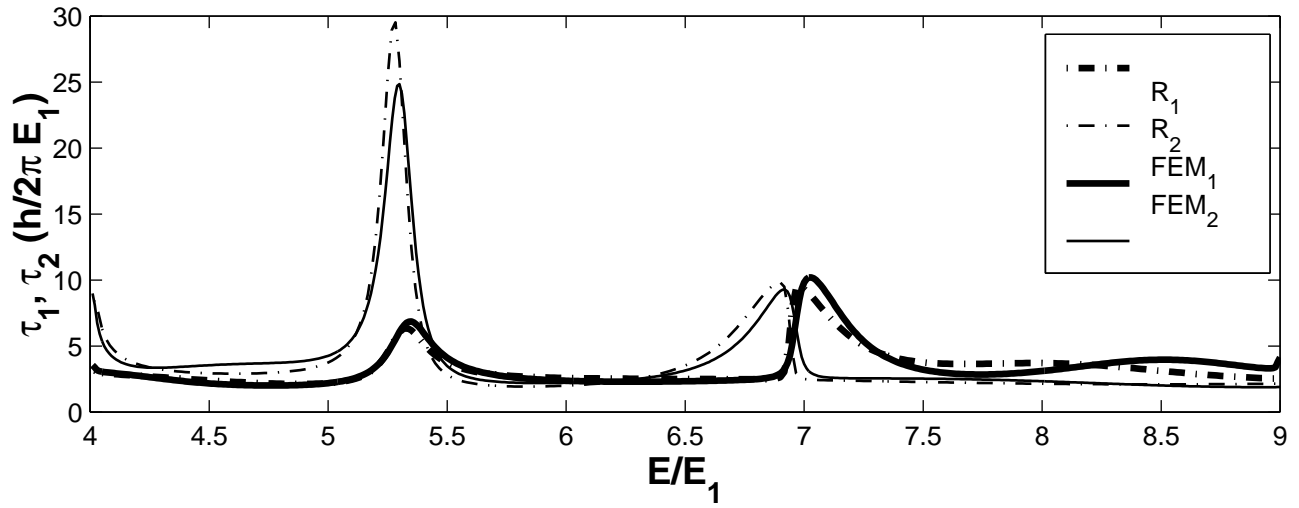
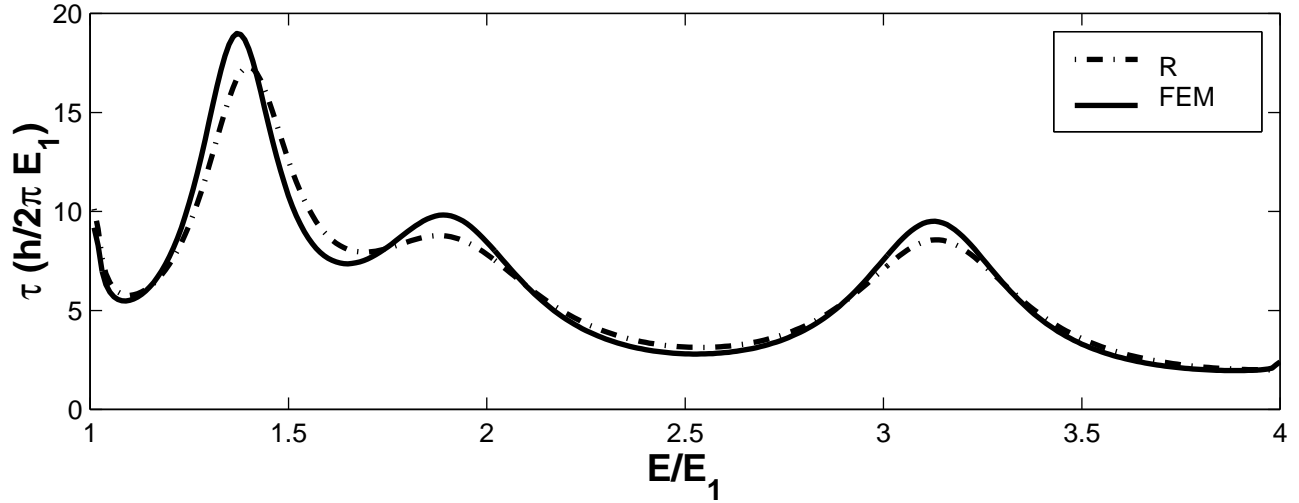


Fig.3. G.B. Akguc and L.E. Reichl



This figure "fx4.jpg" is available in "jpg" format from:

<http://arxiv.org/ps/nlin/0012027v1>

Fig.5, G.B. Akguc and L.E.Reichl

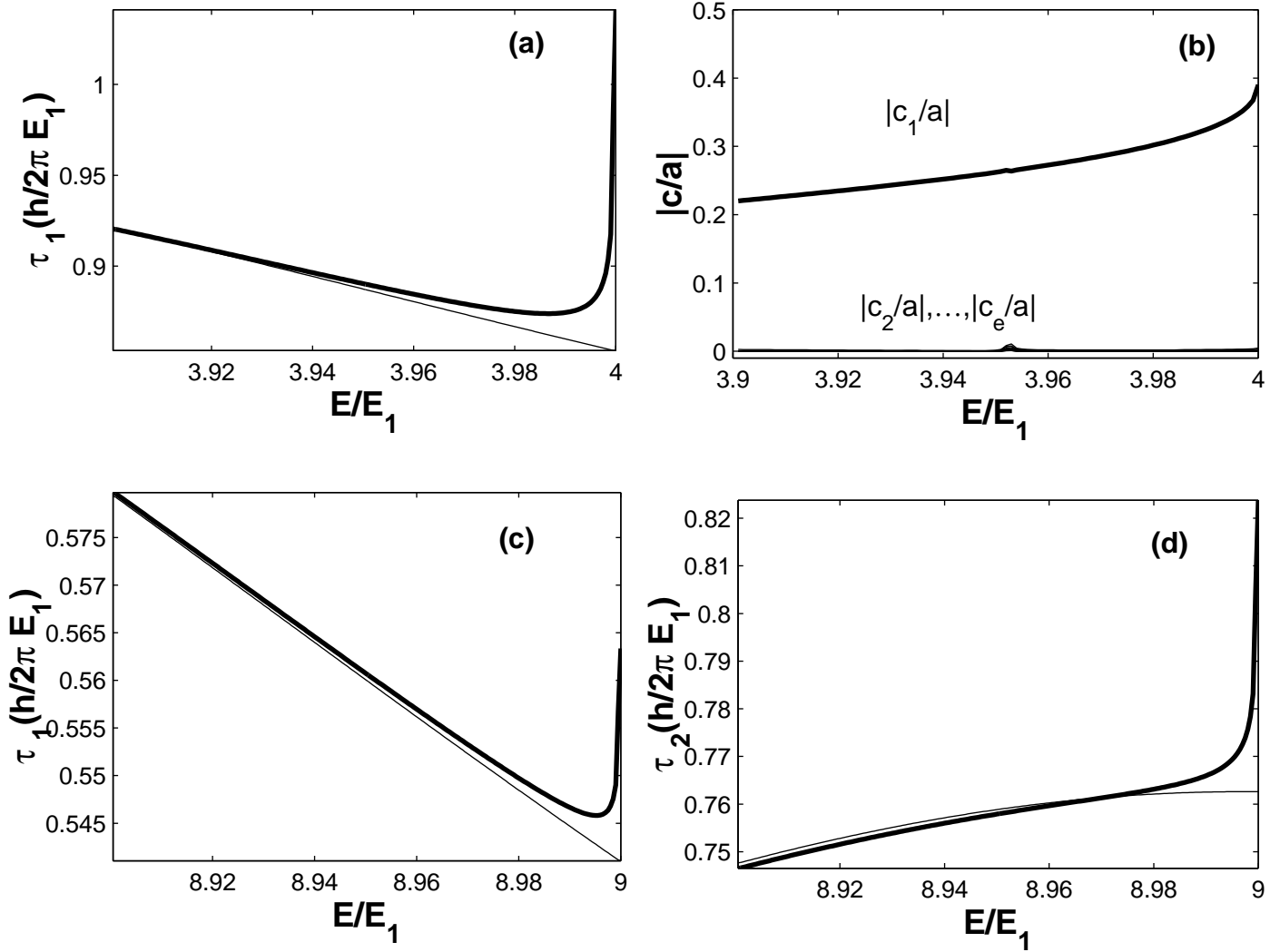


Fig.6, G.B. Akguc and L.E.Reichl

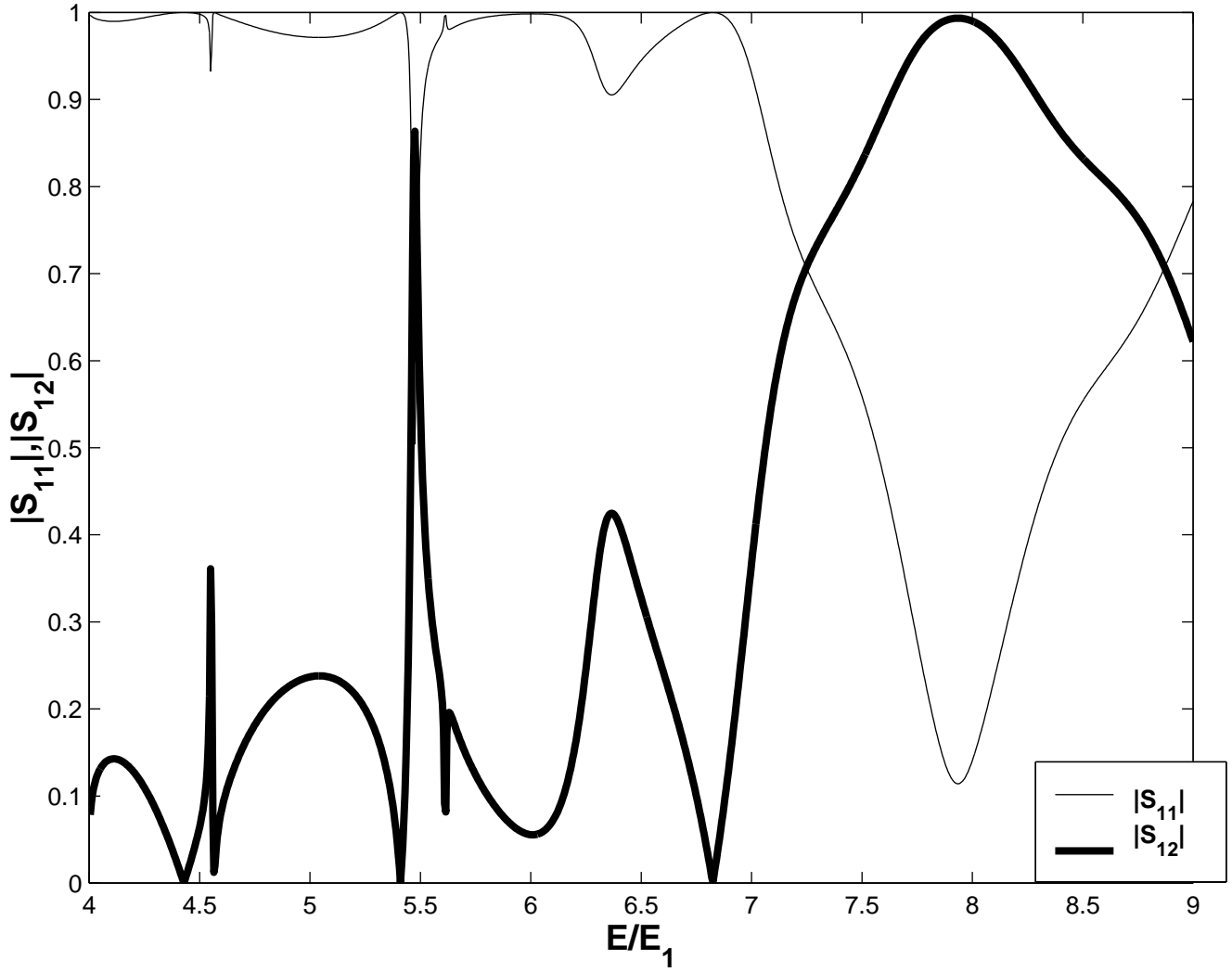
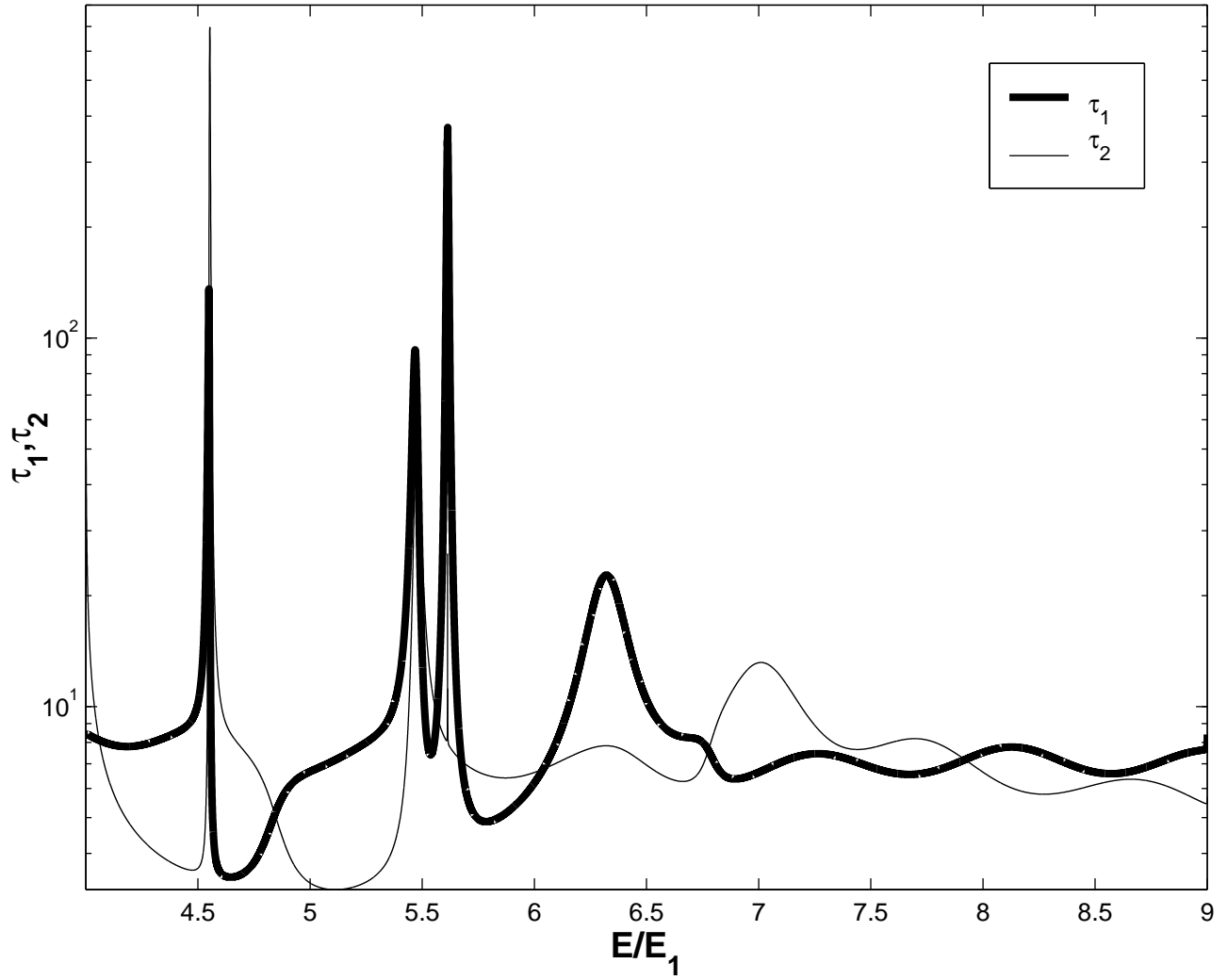


Fig.7, G.B. Akguc and L.E.Reichl



This figure "fx8.jpg" is available in "jpg" format from:

<http://arxiv.org/ps/nlin/0012027v1>

Fig.9, G.B. Akguc and L.E. Reichl

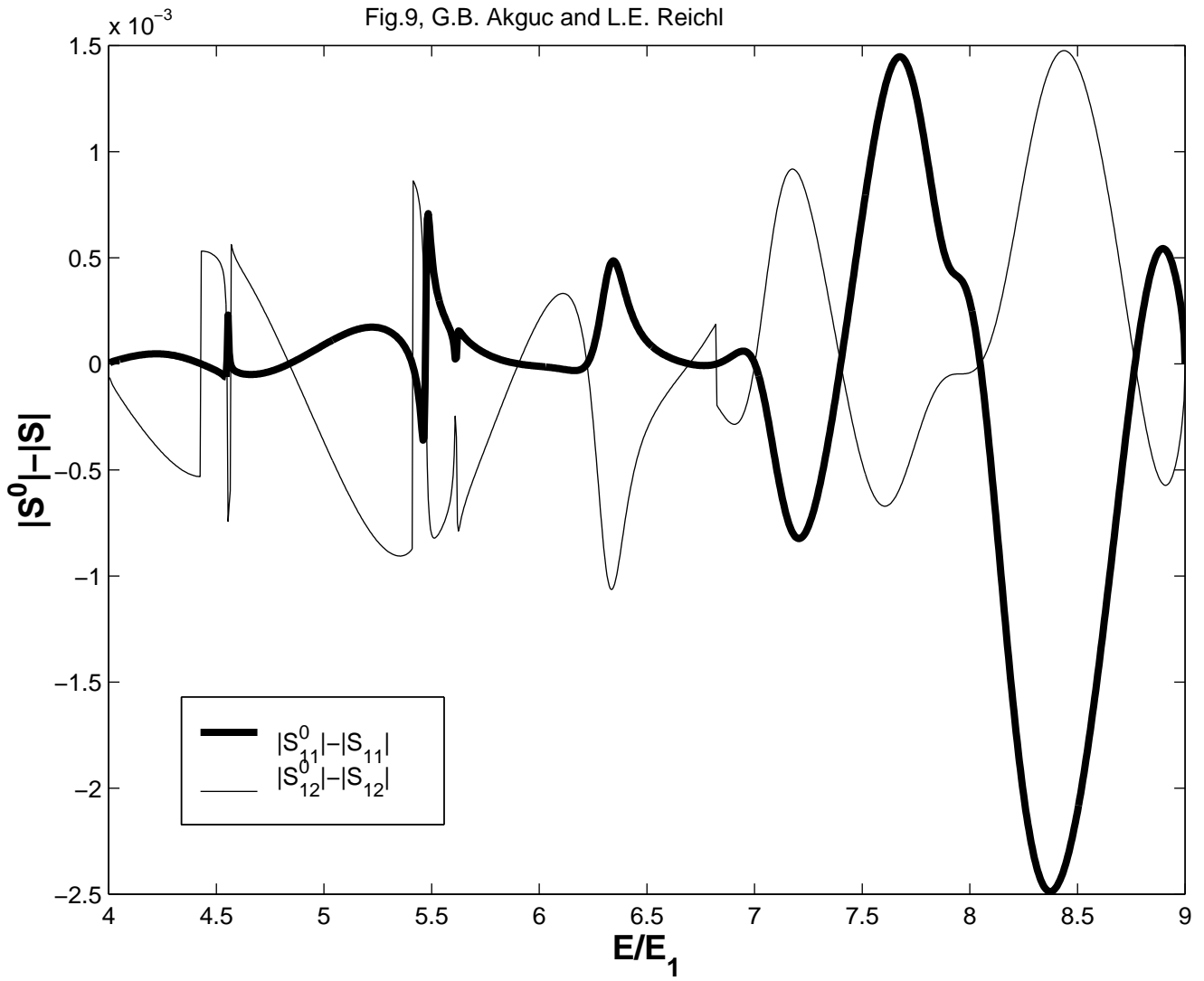
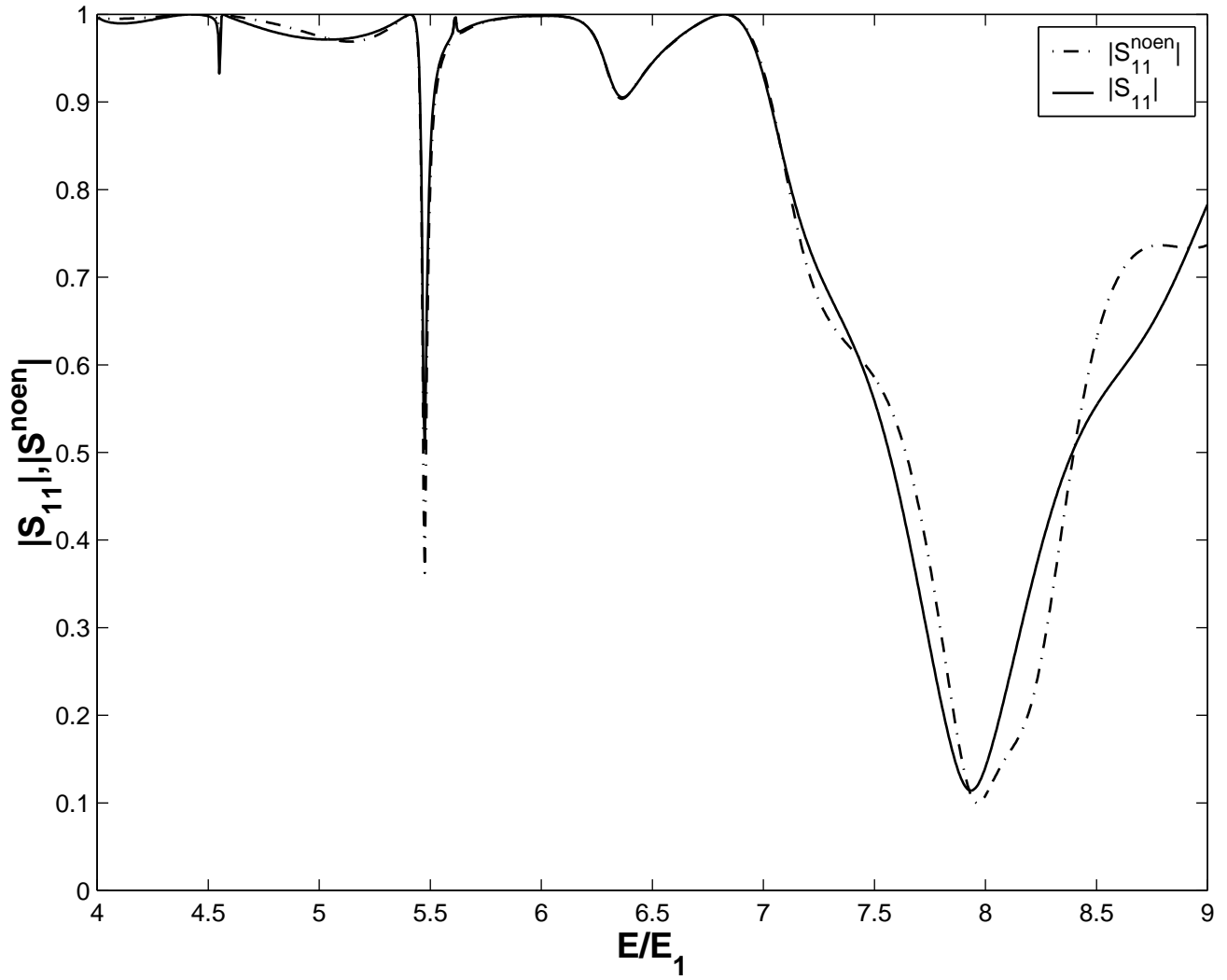


Fig.10, , G.B. Akguc and L.E.Reichl



This figure "fx11.jpg" is available in "jpg" format from:

<http://arxiv.org/ps/nlin/0012027v1>

This figure "fx12.jpg" is available in "jpg" format from:

<http://arxiv.org/ps/nlin/0012027v1>